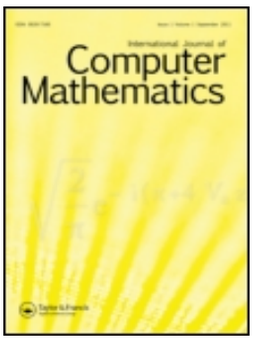

International Journal of Computer Mathematics

ISSN: 0020-7160 (Print) 1029-0265 (Online) Journal homepage: https://www.tandfonline.com/loi/gcom20

A numerical study of a heart phantom model

Y. Zhu, X.Y. Luo, H. Gao, C. McComb & C. Berry

To cite this article: Y. Zhu, X.Y. Luo, H. Gao, C. McComb & C. Berry (2014) A numerical study of a heart phantom model, International Journal of Computer Mathematics, 91:7, 1535-1551, DOI: 10.1080/00207160.2013.854337

To link to this article: https://doi.org/10.1080/00207160.2013.854337

International Journal of Computer Mathematics, 2014
Vol. 91, No. 7, 1535–1551, http://dx.doi.org/10.1080/00207160.2013.854337

Taylor & Francis
Taylor & Francis Group

A numerical study of a heart phantom model

Y. Zhu[a]*, X.Y. Luo[a], H. Gao[a], C. McComb[b] and C. Berry[b]

[a]*School of Mathematics and Statistics, University of Glasgow, Glasgow G12 8QW, UK;* [b]*Institute of Cardiovascular and Medical Sciences, BHF Glasgow Cardiovascular Research Centre, University of Glasgow, Glasgow, UK*

(*Received 30 April 2013; revised version received 17 July 2013; accepted 5 October 2013*)

In this paper, we develop a computational heart phantom model based on magnetic resonance imaging (MRI) of a dynamic multi-modality heart phantom. The phantom is made of a hydrogel material which mimics the elasticity of human soft tissue, and is composed of anatomically correct left and right ventricle structures. The numerical analysis is carried out using the neo-Hookean constitutive model, and the C++ based object-oriented finite element library libMesh is used to solve the fully nonlinear governing equations. We derive the partial differential equations into a set of Lagrangian mesh, and use the weighted residual Galerkin method and Newton iteration solver in the numerical scheme. To validate the numerical model, the displacements and strains of some representative points are compared with experimental measurements and MRI-based strain estimations. Good agreement is obtained, and limitations of the model are discussed.

Keywords: nonlinear elasticity; large strain; heart phantom; MRI; neo-Hookean

2010 AMS Subject Classifications: 74G15; 74B20; 65Z05; 65Y20

1. Introduction

The relationships between heart disease and pump function and dysfunction remain incompletely understood. Since heart disease is a major global cause of morbidity and mortality, new and improved diagnostic and treatment approaches remain a priority for healthcare providers worldwide. Although echocardiography is widely used for heart imaging, cardiac magnetic resonance imaging (MRI) is especially useful for the identification of high-risk pathological characteristics. For example, in patients with a history of myocardial infarction, cardiac MRI can reveal infarct scar, haemorrhage and oedema, all of which can be linked with function. It has been shown [5,26–28] that MRI is highly informative for assessing heart function, volumes and injury (area-at-risk, scar burden, salvaged myocardium, microvascular obstruction, haemorrhage and thrombus). In fact, infarct pathologies tend to aggregate in the highest risk patients in whom MRI is most informative. Overall, cardiac MRI is the gold standard diagnostic method for imaging the heart for clinical and research purposes.

However, cardiac MRI has some limitations and from a technical perspective, continues to evolve. A clinical MRI scan involves multiple different images of the beating heart which are separately acquired over time. A standard cardiac MRI scan usually lasts around 45 min. In order

*Corresponding author. Email: yzhu016@gmail.com

to provide a report, the clinician must review each of the image sets separately, one after the other. While MR vendor software is typically excellent, there are fundamental inefficiencies in the diagnostic review process since images must be viewed separately and sequentially. Therefore, pathology and function are dissociated meaning information with a scan that can be neither fully understood nor predictive of health outcomes. Therefore, computational heart modelling has the potential to help to overcome some of these problems by integrating discrete MRI data sets to enhance the diagnostic value of the study.

Mechanical models based on simplified left ventricular (LV) geometries can provide basic insights into the finite deformation and transmural stress distributions. Assuming the LV to have thick-walled cylindrical geometry, Humphrey and Yin [14,15] investigated the transmural distribution of stress in the equatorial region of a passive LV based on a constitutive model derived from biaxial experimental data. Since there is a lack of sufficient experimental data, particularly regarding the mechanical properties of myocardium, their computational modelling results must be interpreted cautiously with regard to their physiological implications. Guccione *et al.* [12] modelled the equatorial region of the canine LV as a thick-walled cylinder. The advantage of these simplified models is that it could provide a reasonable approximation of the equatorial region and allows to account for many of nonlinear features of the myocardium without using sophisticated computational techniques such as finite element (FE) analysis. However, measurements of realistic ventricular geometry rather than estimations from simpler models are required if we need to obtain accurate stress and strain distributions [15,25].

The recent development of computational models of the heart has enhanced our understanding of the relationships between heart disease and function [1]. For example, Guccione *et al*. found that myocardial contractility in the infarct border zone is significantly reduced yet associated with elevated myofibre stress, which predisposes to heart failure in the longer term [13,35–37]. Veress *et al.* [32] simulated normal and abnormal motions of the LV using a physiologically based, FE mechanical model, with the aim to enhance the 4-D NURBS-based NCAT phantom. In their mechanical model, the LV myocardium was represented as a transversely isotropic elastic material with fibre. A gated high-resolution CT image set was selected and used for the geometry of the FE method. Including electro-physiology in the heart models enabled us to study effects of cardiac resynchronization therapy on heart function [31], such as pacing sites on failing and non-failing hearts [18,22,24]. Coupled modelling of LV flow and coronary flow also enhanced our understanding of heart function as a pump [23]. The computational advances have also resulted in complex tools for generating personalized biomechanical models; see, e.g. [33,34], which automatically fits an FE model to segmented data of the LV. In addition, the strain-based kinematic cardiac growth models, such as [11,19], which are now able to capture and hypothesize on explanations for physiological responses such as eccentric and concentric growth. Modelling also enables hypotheses for the optimization of the heart structure to be easily investigated. For example, the assumption that the minimization of the cross-fibre to fibre shear strain governs cardiac fibre orientations [20] provides novel insights linking cardiac physiology to mechanistic effects such as stroke work density. These computational models, thereby, play an integral part in the understanding of the patho-physiology and are essential for obtaining improved methods of treatments for a variety of cardiac diseases.

In order to develop a sophisticated computational approach that can integrate with MRI data sets, which have the potential to provide a better understanding of healthy and diseased hearts, we first need to validate the computational framework in simpler scenarios. In this paper, we apply our computational approach to an MRI-derived heart phantom, for which the precise control parameters (i.e. the exact anatomy, the passive material properties of the phantom and the boundary conditions) are known. We use Shelley's dynamic multi-modality anthropomorphic heart phantom (Shelley Medical Imaging Technologies, Ontario), which has been purposely developed as a tool for the analysis and validation of cardiac motion techniques related to medical imaging.

The remainder of the paper is organized as follows. We begin with the process for creating the FE mesh from the MRI images in Section 2, and then we describe the experimental set-up and method for extracting displacement data (Section 3). Details of numerical simulations of the heart phantom model are given in Section 4. Finally, we compare the computational results with experimental measurements and MRI-based strain estimation.

2. MRI-derived phantom geometry

The anthropomorphic heart phantom is shown in Figure 1. The phantom is MRI compatible with computer-controlled left ventricle (LV) and right ventricle (RV) heart motion. The heart phantom is intended for the validation of imaging processing, reconstruction algorithms and interventional guidance/tracking applications.

The phantom is made of a polyvinyl alcohol (PVA) hydrogel material which mimics the elasticity of human soft tissue with anatomically correct LV and RV structures incorporated, see heart phantom reference [8]. MR images were obtained using a 3 Tesla Siemens Verio scanner (Siemens, Erlangen, Germany) with a 6-channel phased-array body coil. An artificial heart rate of 60 bpm was generated by the control system of the heart phantom to enable the MRI protocol to run gated to a simulated ECG recording, and short axis stacks of cine images (see Figure 1(a,b)) covering the entire phantom were acquired using a FLASH sequence with the following parameters: repetition time $= 54.2$ ms, echo time $= 2.9$ ms, field of view $= 162\,\text{mm} \times 200\,\text{mm}$, slice thickness $= 2$ mm without gap and resolution $= 1.3\,\text{mm} \times 1\,\text{mm} \times 2\,\text{mm}$.

A total of 37 short axis slices were chosen for phantom geometry reconstruction. First, a recursive Gaussian filter was applied to reduce the noise ($\sigma = 1.4$ mm). Second, the MR images were segmented by a threshold operator in the Simpleware ScanIP package (Simpleware Ltd, Exeter, UK). Third, morphological operations were used to fill cavities, remove artefacts and

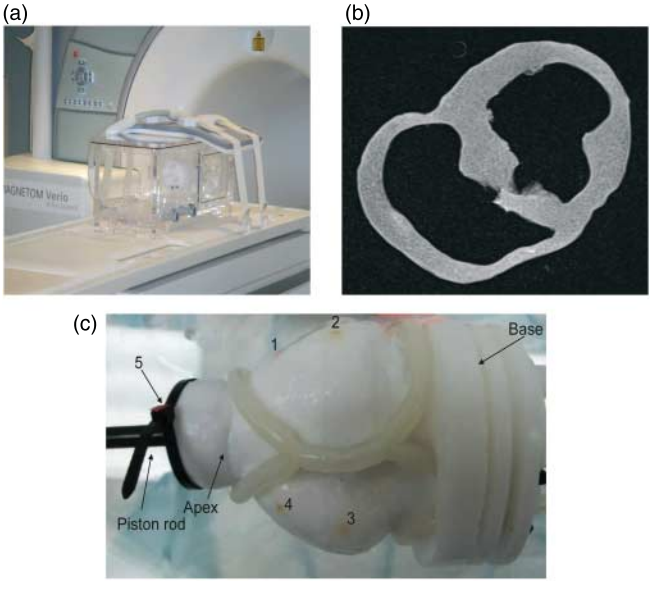

Figure 1. Experimental set-up of the heart phantom. (a) The heart phantom sitting in the water tank. (b) One short axis MRI slice. (c) A close view of the heart phantom with the apex plane (left) moving in a prescribed motion. The apex plane is defined by the circular disk attached to the apex area of the heart phantom. The marked points 1–4 are used for comparison with numerical simulations, the marker 5 is used for extracting the apex motion.

isolated objects. Manual editing was performed to correct minor errors if necessary. Finally, the reconstructed heart phantom model was exported into the Cubit Geometry and Mesh Generation Tool Suite (http://cubit.sandia.gov), where the tetrahedral mesh was generated.

3. Experimental set-up

Two servomotors and an actuator were connected to the hydrogel heart phantom allowing for control of compression, stretching and torsion motion of tissue deformation. The motion of the heart phantom was driven by the piston and the piston rod system: the apex part of the heart phantom rotated around the centre of the piston rod and at the same time moved forward or backward in the long axis direction, see Figure 1(c). We remarked that in this system, there was no flow flux being pushed by the piston into the phantom – unlike in the real heart; therefore, the phantom motion was entirely driven by the time-dependent displacement and twist provided to the apex.

We considered two scenarios with different driven pressures, 20 psi (137.9 kPa) and 40 psi (275.8 kPa), respectively, referred to as cases A and B. Again, the pressure was used to control the motion of the apex of the heart phantom, it is not the hydrostatic pressure applied inside the LV and RV. Since the heart phantom was set to beat 60 times per minute in experiments, the simulation time of both cases was set to 1 s, which was equal to the period of one phantom cycle.

To extract the displacements from the phantom heart, two digital cameras were used to follow five markers embedded in the heart phantom as shown in Figure 1(c), since the markers were not MRI-compatible; therefore, the markers' motion could not be traced using the MRI scanner. Each camera was able to record two-dimensional motions. Our tests showed that the measured motion error was less than 2%.

The marker in 'position 5' provided the completed information of the apex plane. Figure 2 illustrates the process of extracting θ from camera recorded videos. Marker 5 was initially located at position A in un-deformed configuration and moved to position B at time step 1, then the relation of rotational angle θ of marker 5 and the displacement components u, v at time step 1 could be calculated by

$$|BC| = u = r\sin\theta, \quad |AC| = v = r(\cos\theta - 1), \tag{1}$$

where r is the radius of the apex plane. In addition, videos of the beating heart phantom were taken for recording the motion of the apex plane in the long axis direction. Then using similar image processing, we obtained the displacement component w of marker 5, and these results are shown in Figures 3 and 4. These data points were then fitted using a smoothing spline algorithm in Matlab R2010a (The MathWorks Inc, Natick, USA). The clockwise direction (from the apex view) was considered as the positive direction of the rotation θ.

4. The numerical model

4.1 *Nonlinear equations*

In the reference configurations we describe points of the phantom in terms of the position vector $\mathbf{X}$, while in the deformed configuration of the phantom, the position vector of the material point is denoted by $\mathbf{x}$. We describe the deformation in the form

$$\mathbf{x} = \mathbf{X} + \mathbf{u}, \tag{2}$$

where $\mathbf{u} = \mathbf{u}(\mathbf{X})$ is the displacement vector.

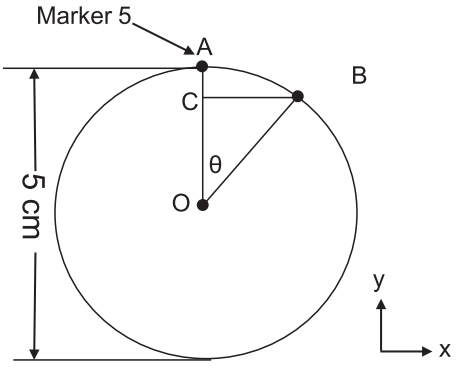

Figure 2. Illustration of extracted displacements from apex plane.

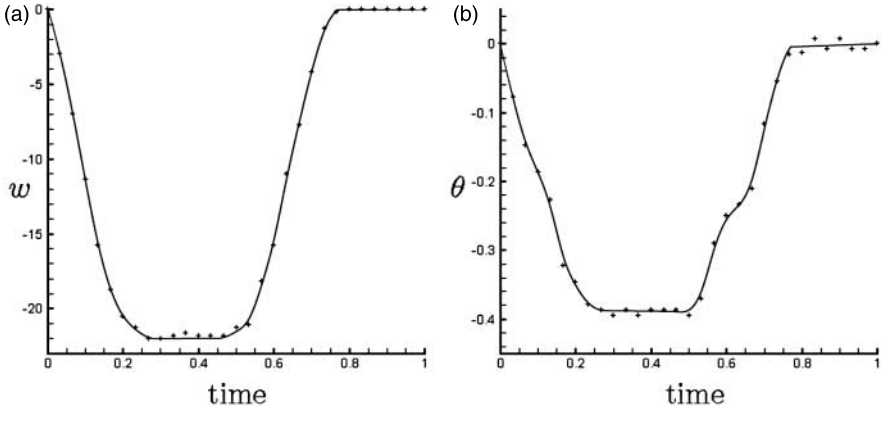

Figure 3. The motion of the apex plane for case A. The symbol (+) indicates the raw data obtained from camera recordings, fitted with splines. (a) Displacements (mm) in the long axis direction versus time (s), and (b) rotational angle θ (radian) versus time (s).

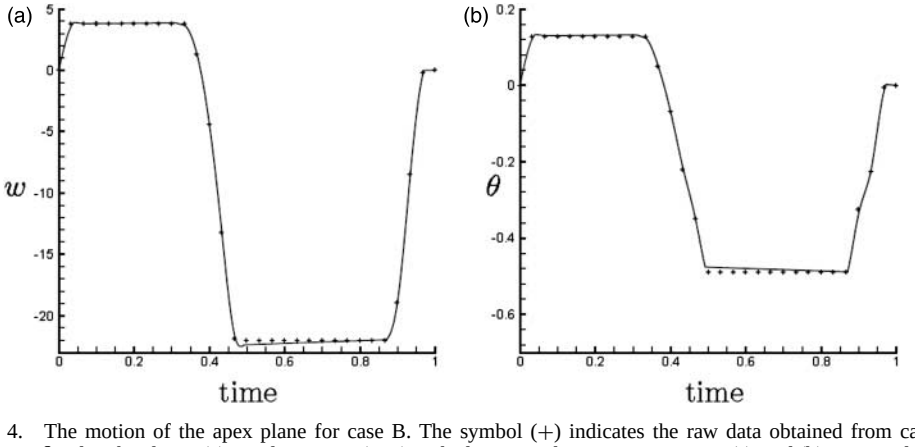

Figure 4. The motion of the apex plane for case B. The symbol (+) indicates the raw data obtained from camera recordings, fitted with splines. (a) Displacements (mm) in the long axis direction versus time (s), and (b) rotational angle θ (radian) versus time (s).

With respect to the chosen bases, the deformation gradient tensor $\mathbf{F}$ may be written as

$$\mathbf{F} = \mathrm{Grad}\,\mathbf{x} = \frac{\partial x_i}{\partial X_j}\mathbf{e}_i \otimes \mathbf{E}_j, \tag{3}$$

where $\mathbf{e}_i$ $(i = 1, 3)$ are the Cartesian unit basis vectors in the current configuration and $\mathbf{E}_j$ $(j = 1, 3)$ are the basis vectors in the reference configuration. Note summation over indices i and j from 1 to 3 is implied. The phantom material is incompressible, hence

$$\det \mathbf{F} = 1. \tag{4}$$

For an incompressible hyperelastic material with strain-energy function $W = W(\mathbf{F})$ per unit volume, the nominal stress tensor $\mathbf{S}$ is given by

$$\mathbf{S} = \frac{\partial W}{\partial \mathbf{F}} - p\mathbf{F}^{-1}, \tag{5}$$

where p is a Lagrange multiplier associated with constraint (4). In the absence of body forces, the equilibrium equation is expressed in terms of the nominal stress as

$$\mathrm{Div}\,\mathbf{S} = \mathbf{0}, \tag{6}$$

where Div is the divergence operator with respect to $\mathbf{X}$. The Cauchy stress tensor $\boldsymbol{\sigma}$ for an incompressible material is related to $\mathbf{S}$ by $\boldsymbol{\sigma} = \mathbf{FS}$, and Equation (6) may be written equivalently as $\mathrm{div}\,\boldsymbol{\sigma} = \mathbf{0}$.

Since the material of the phantom is PVA hydrogel, it can be described using rubber elasticity [3], as for most polymeric materials. We use the neo-Hookean strain-energy function W for the hydrogel,

$$W = \tfrac{1}{2}\mu(I_1 - 3), \tag{7}$$

where the constant μ is the shear modulus of the material and $I_1 = \mathrm{tr}\,(\mathbf{F}^{\mathrm{T}}\mathbf{F})$. To estimate the shear modulus, the phantom material is tested in a simple uni-axial stretching test. Three material samples have been tested, the mean value of Young's modulus is E is 110.25 ± 0.49 kPa. The corresponding shear modulus $\mu = E/3 = 36.75$ kPa.

4.2 *FE algorithm*

4.2.1 *FE equations*

The governing PDEs (6) and the constraint equation (4) are approximated by using the weighted residual Galerkin method, with the elastic domain divided into a set of sub-domains. In terms of quadratic shape functions N_k and linear shape functions L_k, the displacement components (u, v, w) and the Lagrange multiplier p are written as

$$u = \sum_{k=1}^{n_1} N_k(\xi, \eta)u_k, \quad v = \sum_{k=1}^{n_1} N_k(\xi, \eta)v_k, \quad w = \sum_{k=1}^{n_1} N_k(\xi, \eta)w_k, \quad p = \sum_{k=1}^{n_2} L_k(\xi, \eta)p_k,$$

where n_1 and n_2 are the element node numbers, which are dependent on the element type chosen, ξ and η are natural coordinate variables, corresponding to isoparametric FEs, u_k, v_k, w_k are the components of the displacement at node k and p_k is the Lagrange multiplier at node k.

Using Equations (4)–(6), the discretized FE equations to be solved are

$$\mathfrak{R} \equiv \mathcal{K}(\mathbf{U})\mathbf{U} - \mathcal{F}(\mathbf{U}) = \mathbf{0}, \tag{8}$$

where $\mathbf{U}$ is the global vector of unknowns, $\mathcal{K}(\mathbf{U})$ is the global stiffness matrix, $\mathcal{F}(\mathbf{U})$ denotes the force vector, which is also dependent on $\mathbf{U}$, and $\mathfrak{R}$ is the global residual vector. To avoid distorted elements in the deformation of the phantom geometry, tetrahedral elements are used in the simulations. The nonlinear partial differential equations are solved with the help of the open-source FE library [20], which can be used as an interface to the high-quality software PETSc (http://www.mcs.anl.gov/petsc), a linear systems solver on both serial and parallel platforms.

4.2.2 *Mixed displacement/pressure formulation*

For incompressible or nearly incompressible materials, a pure displacement-based procedure is in general not effective and produce results showing stiffness far greater than would be expected, rendering the results useless. This particular problem is called locking. To overcome this problem, we used a mixed displacement/pressure formulation to solve the fully nonlinear equilibrium equations. Since the magnitude of displacement w increases sharply in a relatively short time interval, relatively small incremental of displacements have to be used. We now summarize the details of the discretization and the numerical techniques used. The matrix equation (8) is assembled from the FE matrix equations, which are

$$\begin{aligned}
&\sum_{j=1}^{n_1} \int_{\Omega^e} \mu(N_{i,1}N_{j,1} + N_{i,2}N_{j,2} + N_{i,3}N_{j,3})\,\mathrm{d}\Omega^e u_j \\
&\quad + \sum_{j=1}^{n_1} \int_{\Omega^e} p\{N_{i,1}[-(1+w_{,3})N_{j,2} + w_{,2}N_{j,3}] + N_{i,2}[-w_{,1}N_{j,3} + (1+w_{,3})N_{j,1}] \\
&\quad + N_{i,3}(-w_{,2}N_{j,1} + w_{,1}N_{j,2})\}\,\mathrm{d}\Omega^e v_j + \sum_{j=1}^{n_1} \int_{\Omega^e} p(-N_{i,1}N_{j,3} + N_{i,3}N_{j,1})\,\mathrm{d}\Omega^e w_j \\
&\quad - \sum_{j=1}^{n_2} \int_{\Omega^e} N_{i,1}L_j\,\mathrm{d}\Omega^e p_j + \int_{\Omega^e} \mu N_{i,1}\,\mathrm{d}\Omega^e = 0,
\end{aligned} \tag{9}$$

$$\begin{aligned}
&\sum_{j=1}^{n_1} \int_{\Omega^e} p\{N_{i,1}[-w_{,2}N_{j,3} + (1+w_{,3})N_{j,2}] + N_{i,2}[-(1+w_{,3})N_{j,1} + w_{,1}N_{j,3}] \\
&\quad + N_{i,3}(-w_{,1}N_{j,2} + w_{,2}N_{j,1})\}\,\mathrm{d}\Omega^e u_j + \sum_{j=1}^{n_1} \int_{\Omega^e} \mu(N_{i,1}N_{j,1} + N_{i,2}N_{j,2} + N_{i,3}N_{j,3})\,\mathrm{d}\Omega^e v_j \\
&\quad + \sum_{j=1}^{n_1} \int_{\Omega^e} p(-N_{i,2}N_{j,3} + N_{i,3}N_{j,2})\,\mathrm{d}\Omega^e w_j - \sum_{j=1}^{n_2} \int_{\Omega^e} N_{i,2}L_j\,\mathrm{d}\Omega^e p_j + \int_{\Omega^e} \mu N_{i,2}\,\mathrm{d}\Omega^e = 0,
\end{aligned} \tag{10}$$

$$\begin{aligned}
&\sum_{j=1}^{n_1} \int_{\Omega^e} p[N_{i,1}(1+v_{,2})N_{j,3} - N_{i,2}v_{,1}N_{j,3} - N_{i,3}(1+v_{,2})N_{j,1}]\,\mathrm{d}\Omega^e u_j \\
&\quad + \sum_{j=1}^{n_1} \int_{\Omega^e} p[-N_{i,1}u_{,2}N_{j,3} + N_{i,2}(1+u_{,1})N_{j,3} + N_{i,3}(-N_{j,2} + u_{,2}N_{j,1})]\,\mathrm{d}\Omega^e v_j
\end{aligned}$$

$$+\sum_{j=1}^{n_1}\int_{\Omega^e}\mu(N_{i,1}N_{j,1}+N_{i,2}N_{j,2}+N_{i,3}N_{j,3})\,\mathrm{d}\Omega^e w_j$$

$$-\sum_{j=1}^{n_2}\int_{\Omega^e}N_{i,3}L_j\,\mathrm{d}\Omega^e p_j+\int_{\Omega^e}\mu N_{i,3}\,\mathrm{d}\Omega^e=0, \tag{11}$$

$$\sum_{j=1}^{n_1}\int_{\Omega^e}L_i[(1+v_{,2}+w_{,3}+v_{,2}w_{,3}-v_{,3}w_{,2})N_{j,1}+(v_{,3}w_{,1}-v_{,1}-v_{,1}w_{,3})N_{j,2}$$

$$+(v_{,1}w_{,2}-w_{,1}-v_{,2}w_{,1})N_{j,3}]\,\mathrm{d}\Omega^e u_j+\sum_{j=1}^{n_1}\int_{\Omega^e}L_i(N_{j,2}-w_{,2}N_{j,3}+w_{,3}N_{j,2})\,\mathrm{d}\Omega^e v_j$$

$$+\sum_{j=1}^{n_1}\int_{\Omega^e}L_iN_{j,3}\,\mathrm{d}\Omega^e w_j=0, \tag{12}$$

where Ω^e is the domain of an element in the reference configuration, Γ^e is its boundary, $_{,k}$ signifies differentiation with respect to the reference coordinate X_k.

4.2.3 *Displacement boundary conditions*

The Cartesian coordinate system was chosen with the origin located in the base plane of the phantom; the $x-y$ plane coincides with the base plane, and the z-axis is perpendicular to the base plane (see Figure 1(c) and Figure 6(a)). We fixed the displacements of the base of the phantom, so that $u=v=w=0$. The motion of the apex plane was prescribed as the displacement boundary conditions. We assumed that the nodes located in the apex plane have the same displacement components w and rotate with the same angular velocity as the marker 5. Then the motion of all the other nodes in the apex plane could be determined by using Equations (1), see Figures 3 and 4. Notice that r in Equation (1) should be replaced as the distance from centre position O to the node considered.

4.2.4 *Grid independence tests and solution convergence*

Convergence analysis was performed first using grid independence tests on several grid resolutions, as well as for two types of elements. The mesh-A included 325,945 4-node tetrahedral elements with 54,291 nodes. The mesh-B included 85,515 10-node tetrahedral elements with nodes 124,382. Comparison of these two meshes showed that the maximum displacements are almost identical and the differences of maximum stresses in the axial direction are less than 3%. As mesh-B had higher order elements and was faster, it has been used in the following simulations.

Equation (8) was solved in LibMesh by employing the SNES library of PETSc [4], which provides a powerful set of numerical routines, including line search and trust region techniques. Newton–Krylov methods constitute the core of the package. The non-symmetric Jacobian matrix was analytically formulated following [38] and was updated at each Newton iteration. Convergence was achieved when the relative residual tolerance $\|\mathfrak{R}(\mathbf{U}_r)\|/\|\mathfrak{R}(\mathbf{U}_0)\|$ (in the l_2 norm) was less than 10^{-8} or the absolute tolerance $\|\mathfrak{R}(\mathbf{U}_r)\|$ was less than 10^{-10}, where $\mathfrak{R}(\mathbf{U}_0)$ is the initial residual. All computations were run on Linux servers, each with dual six-core Intel Xeon X5650 2.67 GHz CPUs (i.e. 24 cores per system) and 32 GB RAM at the School of Mathematics and Statistics, the University of Glasgow.

5. Results

5.1 *Comparison of displacements*

First, the numerical results for markers 1–4 are compared with measured values, which are sitting on the phantom surface (see Figure 1(c)). Since the camera recorded motions are in 2D plane, thus only the displacement components v and w can be extracted and compared with those from the FE analysis for the camera sitting on the top of phantom. Figure 5 shows that there is a good agreement between the experimental and numerical displacements for markers 1–4. The predictions of v at markers 3 and 4 agree very well in the whole cycle, the maximum displacement w is slightly under-estimated by the numerical model, which might be because that the phantom base plane is fixed in the numerical model, but it moves slightly in the experimental settings due to the effects of material deformation there.

Comparison of our results with the commercial FE package ABAQUS is shown in Figure 5, using the same material model, mesh and boundary conditions. The results from these two simulation models are almost identical.

Figure 6 illustrates the un-deformed and deformed heart phantom under extension and rotation. The largest extensions for both cases are $|w| = 22$ mm. The largest rotations for the two cases were $\theta = 22.6^\circ$ and $\theta = 38.7^\circ$ respectively. The parts of the two ventricles close to the apex were subject to the largest deformations (including extension and torsion). For gross comparison, the heart phantom in un-deformed and deformed configurations is shown in Figure 7.

5.2 *Comparison with strains estimated from tagged MRIs*

In order to compare the predicted strain with experimental data, we use the estimated strains from MRI by applying the B-spline deformable image registration method (BSDIR) to a series of long-axis tagged MR images [2].

The basic idea of the BSDIR method [29] is to find the optimized free-form displacement vector field which can relate each pixel in one image to its position in the other, which is able to map the movement of a structure from one time step to the next time step. From the continuous displacement vector field, strain data can be derived by using continuum mechanical theory. The Cartesian components of Green strains are transformed to the cylindrical coordinate system. Since the current BSDIR method can only be applied to 2D images; therefore, we only estimate strain components E_{rr} and E_{zz} with long axis tagged MR images.

The average strain curves at the selected regions A and B are computed and compared with that of BSDIR. For both strains E_{rr} and E_{zz}, there is a reasonable agreement, though slight discrepancy exists. The reasons for the difference are partially due to (a) BSDIR applies regularization and smoothness to the displacement field, which could over smooth the displacement field, and underestimate strains for the regions with large and fast motion; (b) BSDIR is also affected by the image quality; (c) the tracked position from one image to another by the BSDIR method may not actually be the same physical point. Indeed, it is of the current research challenge to estimate 3D strains from 2D MR images accurately. Having said this, the overall agreement of strain estimated by the model and the BSDIR is encouraging.

5.3 *Stress and strains*

One of the advantages of the computational heart model is that it can provide additional information that is not easily measurable in experiments, such as stress. For the phantom heart, the representative stress distributions in Cartesian system for case A are plotted in Figures 10 for

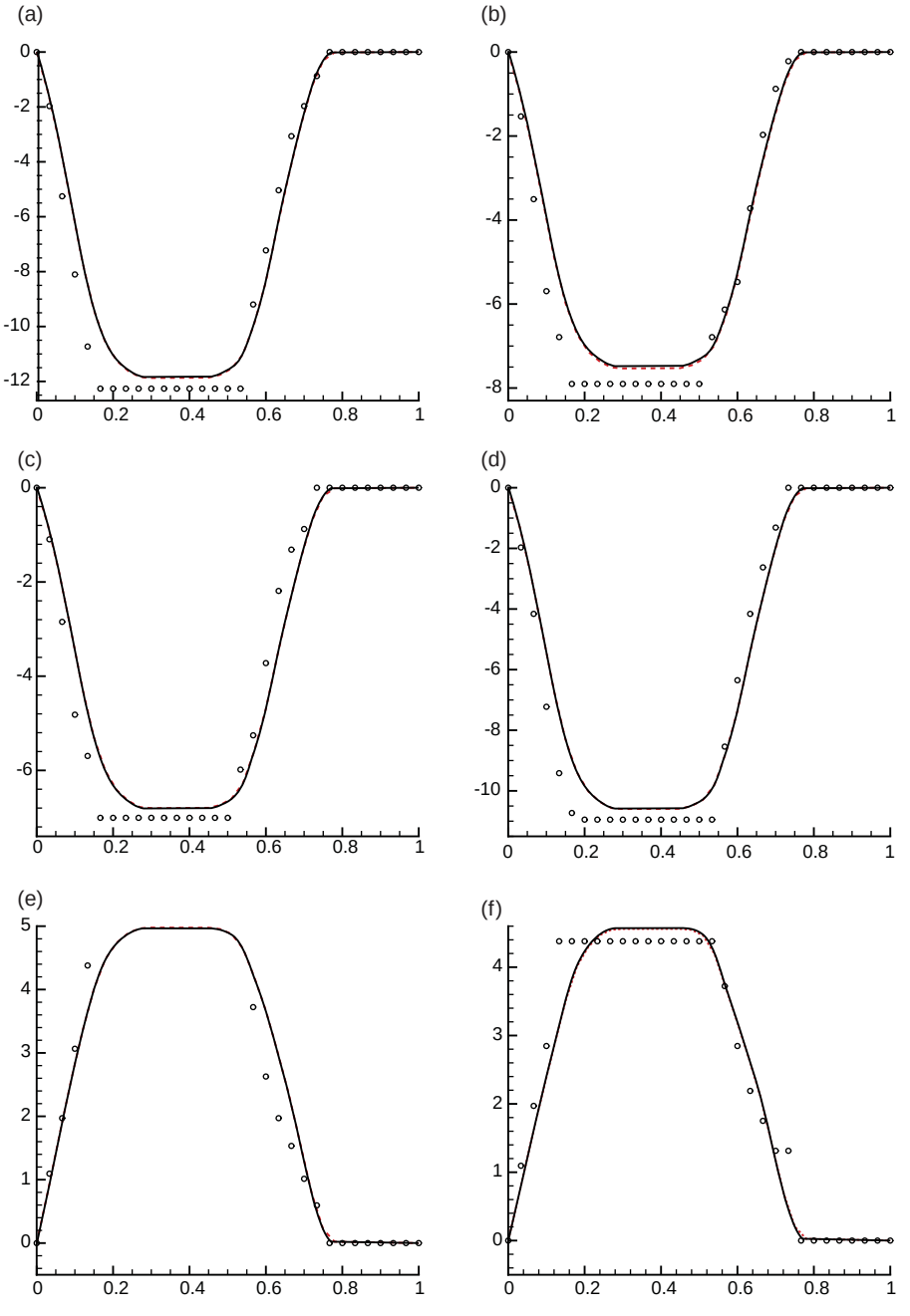

Figure 5. Comparison of the displacement components (mm) v, w at markers 1–4 for Case A. The FE results (black solid lines) are almost identical with those of ABAQUS (dashed lines). Both of the FE results agree well with experimental (circles) results.

$w = -10.08$ mm. It can be seen that the areas of stress concentration are located not only at the base and the apex of the phantom but also at places where the ventricle wall is very thin and where the curvature of the wall surface changes suddenly. We also noted that the magnitude of stress σ_{33} is larger than the other components of the Cauchy stress. All the Cauchy stress components vary significantly between mid-ventricles and the apex.

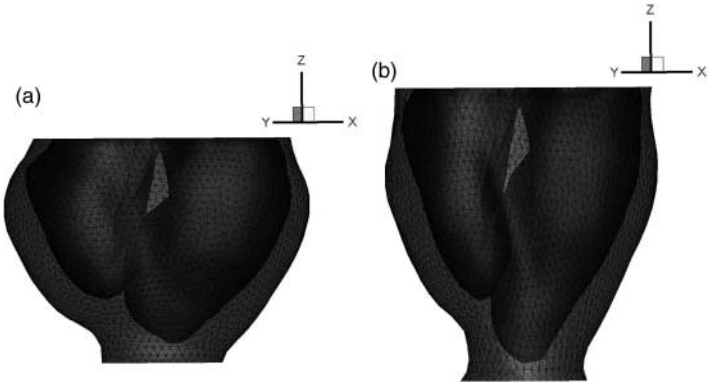

Figure 6. (a) Un-deformed heart phantom and (b) deformed heart phantom at $w = -22$ mm.

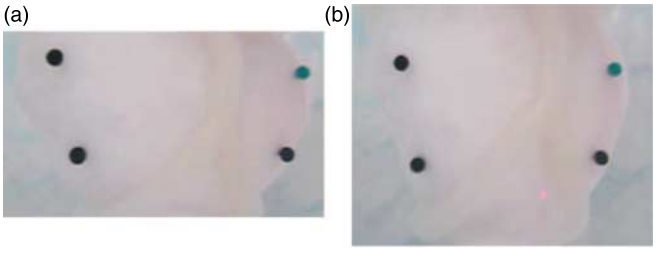

Figure 7. (a) Un-deformed heart phantom and (b) deformed heart phantom at $w = -22$ mm.

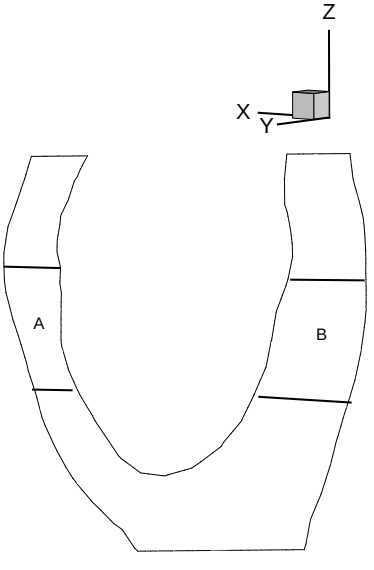

Figure 8. One long axis slice position is chosen for strain comparison between the BSDIR method and the FE model.

From Figure 10, we can see that the magnitudes of the Cauchy stresses are large near the lower boundary of the LV and RV due to the twisting and axial forces exerted there. σ_{22} is negative near the apex of the RV, meaning this part is compressed in the x, y plane. σ_{33} is negative at both the

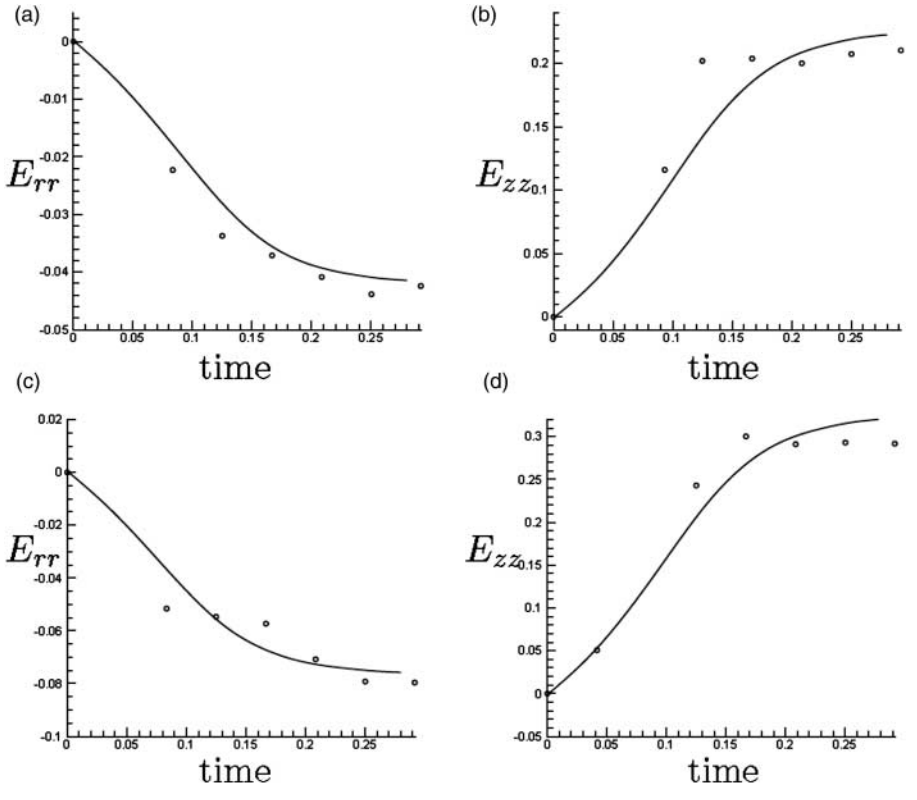

Figure 9. Strain comparisons between the BSDIR method (circle) and FE model (solid line) (a) E_{rr} in sector A, (b) E_{zz} in sector A, (c) E_{rr} in sector B, (d) E_{zz} in sector B in a long axis slice, Sectors A and B are zones near the midventricle. Overall, there is good agreement between the BSDIR method and numerical strains in sectors A and B.

apex of the LV and RV (see Figure 10(c)). Figure 10(c) also shows that σ_{33} is positive in most areas of the section, except when close to the base of the phantom.

Figure 11 illustrates the cavity volumes of the LV and RV in the whole cycle of the motion for cases A and B. The change of cavity volumes for both cases is relatively small, which is defined by

$$\text{Volume changes} = \frac{V_i - V_0}{V_0} \times 100\%, \tag{13}$$

where V_i denotes the volume at the ith time step and V_0 is the initial volume in the reference configuration. For case A, both the cavity volumes are increased up to 4.13% for LV and 5.38% for RV. For case B, both the cavity volumes decrease to -0.42% and -0.88% and then increase up to 4.28% and 5.56%, respectively.

Figure 12 shows the displacement u plotted along three different paths (defined as Paths 1, 2 and 3), across the phantom wall, see Figures 12–14.

Figure 13 reveals that the components of the Green strain vary from endocardium to epicardium. The magnitude of Green strain E_{zz} is much larger compared with other components. Along paths 1, 2 and 3, E_{zz} decreases from endocardium to epicardium while E_{rr} increases from endocardium to epicardium. Along path 1, the curves for all strain components are almost straight lines. E_{rr}, E_{zz} and $E_{r\theta}$ change dramatically from endocardium to epicardium, while $E_{\theta\theta}$, E_{rz} and $E_{\theta z}$ do not change much.

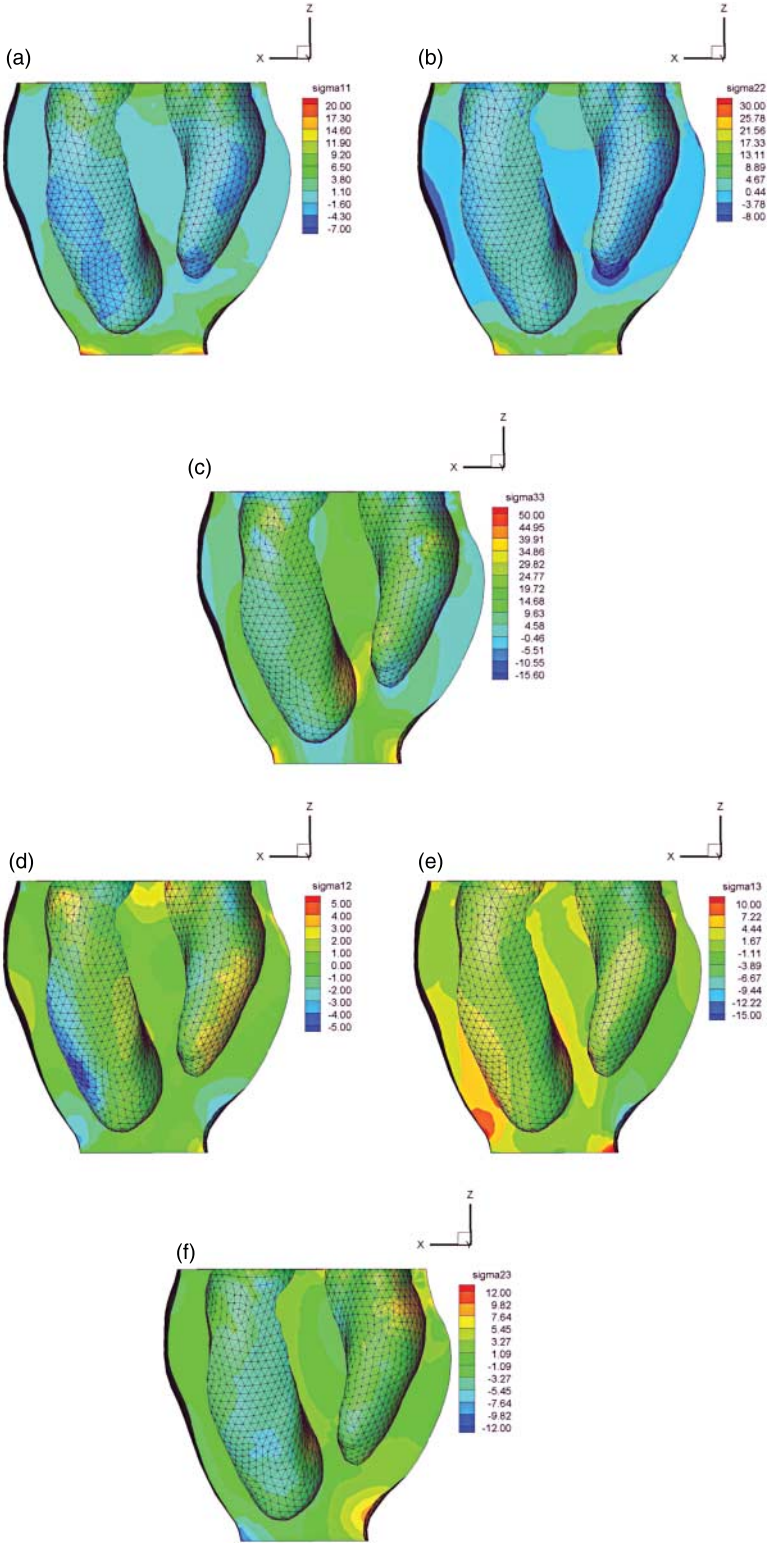

Figure 10. Transmural Cauchy stress components distribution for case A (kPa).

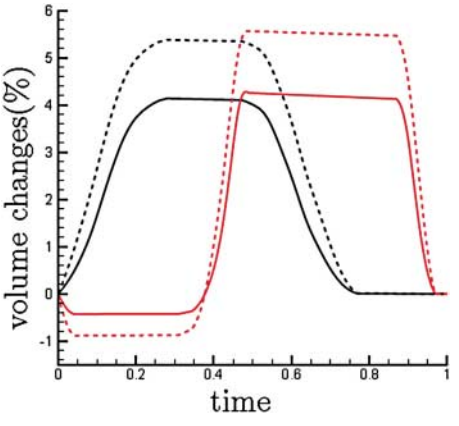

Figure 11. Plot of the left (solid lines) and right (dotted lines) ventricle volume versus time (s). Case A (left, black) and case B (right, red online).

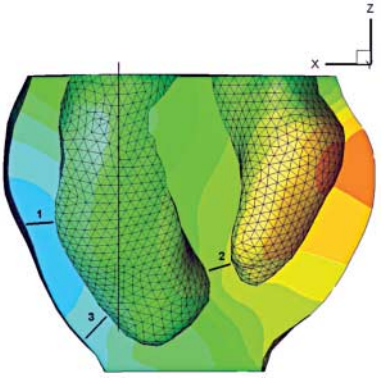

Figure 12. Position of the *z*-axis (for cylindrical strains and stresses) and transmural paths for LV with the distribution of displacement component *u* superimposed.

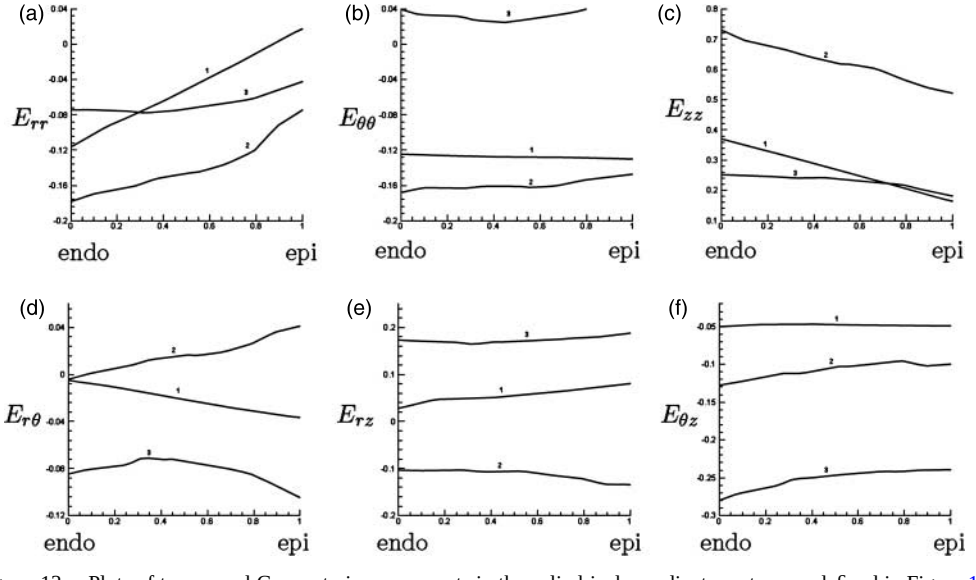

Figure 13. Plots of transmural Green strain components in the cylindrical coordinate system, as defined in Figure 12, along paths 1, 2, 3, when $w = -22.0$ mm, case A.

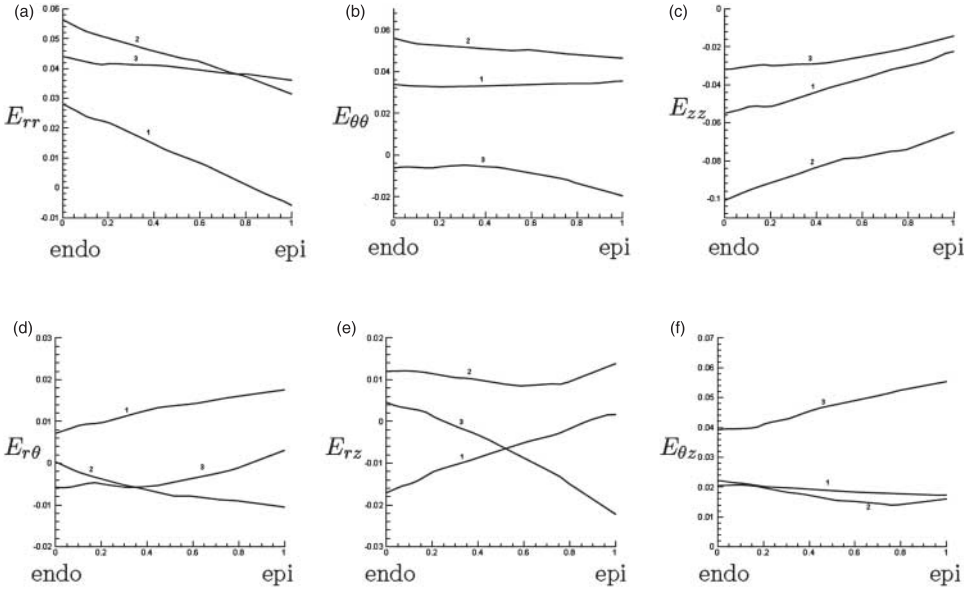

Figure 14. Plots of transmural Green strain components (in cylindrical coordinate system) at position 1, 2, and 3. Case B at $w = 3.9$ mm.

Figure 14 shows the transmural Green strain components at $w = 3.9$ mm for case B. The magnitudes of the strains are small. The curves along the three paths have the similar trend with case A, i.e. the transmural distributions vary monotonically. Compared with Figure 13, the values of E_{rr} and E_{zz} have opposite signs and the absolute magnitude of E_{rr} and E_{zz} decreases almost linearly from endocardium to epicardium.

6. Discussion and conclusions

We have developed an MRI-based computational heart model, and validated the model against Shelley's dynamic multi-dynamic phantom which is MRI compatible. The nonlinear partial differential equations were solved numerically using a in-house code based on the open-sourced FE library libMesh, as well as commercial package ABAQUS. The MRI-based computational model that we have devised will be informative for research into cardiac biomechanics.

In this study, we have shown that our computational approach based on the MRI-derived phantom geometry can successfully simulate the heart phantom motion. There is an excellent agreement in the model and experiments in terms of displacements. We also performed the strain comparison, where the strains are computed, respectively, by the numerical model and the BSDIR method, on a long-axis slice. There was reasonable agreement in strains, both in the trends and the magnitude. However, the BSDIR method is purely based on image analysis, which may contain errors in the recovered strain since the motion is complex; and the image quality is low. Therefore, we only compared two centre regions in the long-axis view. In the future, improvements are needed with MRI method for strain estimation in order to enhance the validation of computational models.

The stress analysis using the phantom model shows that the areas of stress concentration are located not only at the base and the apex of the phantom but also at places where the ventricle wall is very thin and where the curvature of the wall surface changes suddenly. All the Cauchy stress components vary significantly between mid-ventricles and the apex.

Having now evaluated the mechanical phantom used in this project, we conclude that it has limited applicability to model physiological heart motion. This is because motion in the phantom heart model mainly involves extension/compression and twist only, which is incompletely representative of *in vivo* cardiac physiology. In other words, the displacement boundary condition is applied on the apex plane as the driving force to control the motion of the phantom. The motion of heart phantom is far from that of an actual heart. The *in vivo* cardiac cycle is coordinated by a series of electrical impulses that are produced by specialized heart cells leading to cyclical contraction and relaxation mediated by calcium-dependent excitation coupling. Other differences between the heart phantom and real life include differences in blood flow, pressure (intra-cardiac and extra-cardiac), chamber structure and material properties (i.e. the hydrogel material is very different due to the myocardial tissue). Therefore, the stress analysis of the model is only for demonstrative purposes; the stress pattern bears no analogy to that of the physiological heart, which requires more sophisticated constitutive models that account for the muscle fibre direction, myocyte sheet structure of the myocardium and its anisotropic properties. Many constitutive models of the myocardium are available in the literature, including isotropic models [7], transversely isotropic models [13,14,16] and orthotropic models [6,17,30]. It is relatively easy to implement, and indeed we have implemented, more advanced structure-based constitutive heart models in the framework developed here [9,10,33,34].

Acknowledgements

This work was supported by project grants from Medical Research Scotland and the Chief Scientist Office, as well as an EPSRC grant (Ref: EP/I029990/1). Professor Berry is supported by a Senior Fellowship from the Scottish Funding Council. We would like to thank Ms Kirsten Lanaghan and Mrs Tracey Steedman for their help with the MRI scans. Special thanks to Prof. Elizabeth Tanner in University of Glasgow for material testing. All simulations were performed on the Linux workstations at the School of Mathematics and Statistics, University of Glasgow.

References

[1] J. Aguado-Sierra, A. Krishnamurthy, C. Villongco, J. Chuang, E. Howard, M. J. Gonzales, J. Omens, D.E. Krummen, S. Narayan, R.C.P. Kerckhoffs, and A.D. McCulloch, *Patient-specific modeling of dyssynchronous heart failure: A case study*, Progress Biophys. Mol. Biol. 107(1) (2011), pp. 147–155.

[2] A. Allan, H. Gao, C. McComb, and C. Berry, Myocardial strain estimated from standard cine MRI closely represents strain estimated from dedicated strain-encoded MRI, *33rd Annual International Conference of the IEEE EMBS*, Boston, MA, August 30–September 3, 2011, pp. 2650–2653.

[3] K. Anseth, C. Bowman, and L. Brannon-Peppas, *Mechanical properties of hydrogels and their experimental determination*, Biomaterials 17 (1996), pp. 1647–1657.

[4] S. Balay, K. Buschelman, V. Eijkhout, W.D. Gropp, D. Kaushik, M.G. Knepley, L.C. McInnes, B.F. Smith, and H. Zhang, *PETSc users manual*, Tech. Rep. ANL-95/11 – Revision 3.0.0, Argonne National Laboratory, 2008.

[5] C. Berry, P. Kellman, A.H. Aletras, C. Mancini, R.J. Lederman, and A.E. Arai, *Characterisation and initial validation of area-at-risk derived by T2-magnetic resonance imaging in acute myocardial infarction*, Circ. Cardiovasc. Imaging 3(5) (2010), pp. 527–535.

[6] K.D. Costa, J.W. Holmes, and A.D. McCulloch, *Modeling cardiac mechanical properties in three dimensions*, Phil. Trans. R. Soc. Lond. A 359 (2001), pp. 1233–1250.

[7] H. Demiray, *Stress in ventricular wall*, J. Appl. Mech. 98 (1976), pp. 194–197.

[8] *Dynamic heart phantom setup and reference guide*, 2009. Available at http://www.simutec.com.

[9] H. Gao, X.Y. Luo, H.M. Wang, C. Berry, and B.E. Griffith, *Verification of an imaging-derived immersed boundary model of left ventricular mechanics with finite element method*, FIMH Conference, London, 2013.

[10] H. Gao, B.E. Griffith, H.M. Wang, C. Berry, and X.Y. Luo, *Imaging-derived immersed boundary model of left ventricular model with active contraction*, FIMH Conference, London, 2013.

[11] S. Göktepe, O.J. Abilez, and E. Kuhl, *A generic approach towards finite growth with examples of athelte's heart, cardiac dilation, and cardiac wall thickening*, J. Mech. Phys. Solids. 58 (2010), pp. 1661–1680.

[12] J.M. Guccione, A.D. McCulloch, and L.K. Waldman, Passive material properties of intact ventricular myocardium determined from a cylindrical model, *J. Biomech. Eng.* 113 (1991), pp. 42–55.

[13] J.M. Guccione, S.M. Moonly, and P. Moustakidis, K.D. Costa, M.J. Moulton, M.B. Ratcliffe, and M.K. Pasque, *Mechanism underlying mechanical dysfunction in the border zone of left ventricular aneurysm: A finite element model study*, Ann. Thoracic Surgery 71 (2001), pp. 654–662.

[14] J.D. Humphrey and F.C.P. Yin, *On constitutive relations and finite deformations of passive cardiac tissue. I. A pseudostrain-energy function*, ASME J. Biomech. Eng. 109 (1987), pp. 298–304.

[15] J.D. Humphrey and F.C.P. Yin, *Constitutive relations and finite deformations of passive cardiac tissue II: Stress analysis in the left ventricle*, Circulation Res. 65 (1989), pp. 805–817.

[16] J.D. Humphrey, R.K. Strumpf, and F.C.P. Yin, *Determination of constitutive relation for passive myocardium. I. A new functional form*, J. Biomech. Eng. 112 (1990), pp. 333–339.

[17] P.J. Hunter, M.P. Nash, and G.B. Sands, *Computational electromechnics of the heart*, in *Computational biology of the heart*, A.V. Panfilov and A.V. Holden, eds., Wiley, Chichester, 1997, pp. 345–407.

[18] R.C.P. Kerckhoffs, A.D. McCulloch, J.H. Omens, and L.J. Mulligan, *Effects of biventricular pacing and scar size in a computational model of the failing heart with left bundle branch block*, Medical Image Anal. 13(2) (2009), p. 362.

[19] R.C.P. Kerckhoffs, J. Omens, and A.D. McCulloch, *A single strain-based growth law predicts concentric and eccentric cardiac growth during pressure and volume overload*, Mech. Res. Commun. 42 (2012), pp. 40–50.

[20] B. Kirk, J.W. Peterson, R.H. Stogner, and G.F. Carey, *LibMesh: A C++ library for parallel adaptive mesh refinement/coarsening simulations*, Eng. Comput. 22 (2006), pp. 237–254.

[21] W. Kroon, T. Delhaas, P. Bovendeerd, and T. Arts, *Computational analysis of the myocardial structure: Adaptation of cardiac myofiber orientations through deformation*, Med. Image Anal. 13 (2009), pp. 346–353.

[22] N.H. Kuijpers, E. Hermeling, P.H. Bovendeerd, T. Delhaas, and F.W. Prinzen, *Modeling cardiac electromechanics and mechanoelectrical coupling in dyssynchronous and failing hearts: Insight from adaptive computer models*, J. Cardiovasc. Translational Res. 5 (2012), pp. 159–169.

[23] C. Michler, A.N. Cookson, R. Chabiniok, E. Hyde, J. Lee, M. Sinclair, T. Sochi, A. Goyal, G. Vigueras, D.A. Nordsletten, and N.P. Smith, *A computationally efficient framework for the simulation of cardiac perfusion using a multi-compartment Darcy porous-media flow model*, Int. J. Num. Methods in Biomed. Eng. 29 (2012), pp. 217–232.

[24] S.A. Niederer, A.K. Shetty, G. Plank, J. Bostock, R. Razavi, N.P. Smith, and C.A. Rinaldi, *Biophysical modeling to simulate the response to multisite left ventricular stimulation using a quadripolar pacing lead*, Pacing Clin. Electrophysiol. 35(2) (2012), pp. 204–214.

[25] C. Olsen, J. Rankin, C. Arentzen, W. Ring, P. McHale, and R. Anderson, *The deformational characteristics of the left ventricle in the conscious dog*, Circ. Res. 49 (1981), pp. 843–855.

[26] A.R. Payne, M. Casey, J. McClure, A. Murphy, R. McGeoch, X. Bi, S. Zuehlsdorff, R. Woodward, A. Saul, K.G. Oldroyd, N. Tzemos, and C. Berry, *Bright blood T2 weighted MRI has higher diagnostic precision and accuracy than dark blood STIR MRI for assessment of the ischemic area-at-risk and myocardial salvage in acute myocardial infarction*, Circ. Cardiovasc. Imaging 4(3) (2011), pp. 210–219.

[27] A.R. Payne*, C.* Berry (*joint first author), P. Kellman, R. Anderson, L.Y. Hsu, M.Y. Chen, A.R. McPhaden, S. Watkins, W. Schenke, V. Wright, R.J. Lederman, A.H. Aletras, and A.E. Arai, *Bright-blood T2-weighted MRI has high diagnostic accuracy for myocardial hemorrhage in myocardial infarction: A preclinical validation study in Swine*, Circ. Cardiovasc. Imaging 4(6) (2011), pp. 738–745.

[28] A.R. Payne*, C.* Berry (*joint first author), A. Doolin, M. McEntegart, M.C. Petrie, M.M. Lindsay, S. Hood, D. Carrick, N. Tzemos, and J.G. Oldroyd, *Microvascular resistance predicts myocardial salvage and remodeling in ST elevation myocardial infarction*, J. American Heart Assoc. 1(4) (2012), e002246.

[29] D. Rueckert, L.I. Sonoda, C. Hayes, D.L.G. Hill, M.O. Leach, and D.J. Hawkes, *Nonrigid registration using free-form deformations: Application to breastMR images*, IEEE Trans. Med. Images 18(8) (1999), pp. 712–721.

[30] H. Schmid, M.P. Nash, A.A Young, and P.J. Hunter, Myocardial material parameter estimation – a comparative study for simple shear, *J. Biomech. Eng.* 128 (2006), pp. 742–750.

[31] C. Tobon-Gomez, N. Duchateau, R. Sebastian, S. Marchesseau, O. Camara, E. Donal, M. Decraene, A. Pashaei, J. Relan, M. Steghofer, P. Lamata, H. Delingette, S. Duckett, M. Garreau, A. Hernandez, K.S. Rhode, M. Sermesant, N. Ayache, C. Leclercq, R. Razavi, N.P. Smith, and A.F. Frangi, *Understanding the mechanisms amenable to CRT response: from pre-operative multimodal image data to patient-specific computational models*, Med. Biol. Eng. Comput. 51(11) (2013), pp. 1235–1250.

[32] A.I. Veress, W.P. Segars, J.A. Weiss, B.M.W. Tsui, and G.T. Gullberg, *Normal and pathological NCAT image and phantom data based on physiologically realistic left ventricle finite-element models*, IEEE Trans. Med. Imaging 25 (2006), pp. 1604–1616.

[33] H.M. Wang, H. Gao, and X.Y. Luo, *Structure-based finite strain modelling of the human left ventricl in diastole*, Int. J. Numer. Meth. Biomed. Engng. 29 (2013), pp. 83–103.

[34] H.M. Wang, X.Y. Luo, R.W. Ogden, B.E. Griffith, H. Gao, C. Berry, and T.J. Wang, *A modified Holzapfel–Ogden law for a residually stressed finite strain model of the human left ventricle in diastole*, Biomech. Modeling Mechanobiol. 13(1) (2014), pp. 99–113.

[35] J. F. Wenk, P. Eslami, Z. Zhang, C. Xu, E. Kuhl, J.H. Gorman, J.D. Robb, M.B. Ratcliffe, R.C. Gorman, and J.M. Guccione, *A novel method for quantifying the in-vivo mechanical effect of material injected into a myocardial infarction*, Ann. Thorac. Surgery 92(3) (2011), pp. 935–941.

[36] J.F. Wenk, K. Sun, Z. Zhang, M. Soleimani, L. Ge, D. Saloner, A.W. Wallace, M.B. Ratcliffe, and J.M., Guccione, *Regional left ventricular myocardial contractility and stress in a finite element model of posterobasal myocardial infarction*, J. Biomech. Eng. 133(4) (2011), 044501.

[37] J.F. Wenk, D. Klepach, L.C. Lee, Z. Zhang, L. Ge, E.E. Tseng, A. Martin, S. Kozerke, J.H. Gorman, R.C. Gorman, and J.M. Guccione, *First evidence of depressed contractility in the border zone of a human myocardial infarction*, Ann. Thorac. Surgery 93(4) (2012), pp. 1188–1193.

[38] Zhu, Y., X.Y. Luo, and R.W. Ogden, *Nonlinear axisymmetric deformations of an elastic tube under external pressure*, Eur. J. Mech. A/Solids 29 (2010) 216–229.